Origin of Magnetic Anisotropy in Nickelocene Molecular Magnet and Resilience of its Magnetic Behavior

Maristella Alessio, Saikiran Kotaru, Goran Giudetti, and Anna I. Krylov[a]

Department of Chemistry, University of Southern

California, Los Angeles, California 90089-0482, USA

[a] Corresponding author: krylov@usc.edu

Robustness of nickelocene's ($NiCp_2$, Cp = cyclopentadienyl) magnetic anisotropy and addressability of its spin states make this molecular magnet attractive as a spin sensor. However, microscopic understanding of its magnetic anisotropy is still lacking, especially when $NiCp_2$ is deposited on a surface to make quantum sensing devices. Quantum chemical calculations of such molecule/solid-state systems are limited to density functional theory (DFT) or DFT+U (Hubbard correction to DFT). We investigate the magnetic behavior of $NiCp_2$ using the equation-of-motion coupled-cluster (EOM-CC) framework. Our first-principle calculations agree well with experimentally derived magnetic anisotropy and susceptibility values. The calculations show that magnetic anisotropy in $NiCp_2$ originates from a large spin-orbit coupling (SOC) between the triplet ground state and the third singlet state, whereas the coupling with lower singlet excited states is negligible. We also considered a set of six ring-substituted $NiCp_2$ derivatives and a model system of the $NiCp_2$/MgO(001) adsorption complex. To gain insight into the electronic structure of these systems, we analyze spinless transition density matrices and their natural transition orbitals (NTOs). The NTO analysis of SOCs explains how spin states and magnetic properties are retained upon modification of the $NiCp_2$ coordination environment and upon its adsorption on a surface. Such resilience of the $NiCp_2$ magnetic behavior supports using $NiCp_2$ as a spin-probe molecule by functionalization of the tip of a scanning tunneling microscope.

I. INTRODUCTION

Molecular magnets have potential applications as building blocks of spin-based memory devices. The individual molecules can be deposited on a surface or self-assembled into 3D architectures, giving rise to scalable magnetic materials.[1–3] Using molecular magnetic units affords high chemical tunability. To be a good magnet, molecule should possess magnetic anisotropy—orientational dependence of the ability to magnetize. Microscopically, magnetic anisotropy originates from a large spin-orbit coupling (SOC) that gives rise to zero-field splitting (ZFS) of the magnetic sublevels.[4]

Such magnetic anisotropy yields slow magnetic relaxation, providing energy levels that are well-defined by their spin S and spin projection M_S quantum numbers and well-separated in energy. Assuming that coherence times are sufficiently long,[5] in order to realize a molecule-based quantum device, its states must then be easy to address by inducing transitions with light or microwave fields.[6,7] Addressability—the ability of controlling such energy levels and generating superposition states—permits initialization, manipulation, and read-out of the individual molecular magnetic units of a quantum algorithm. To develop individually addressable molecular magnets, one should deposit molecules on a surface and then investigate their electronic structure and magnetic behavior with a probing technique.[1,2]

Spin-flip transitions between the magnetic sublevels of the system can be induced by microwaves within an electron paramagnetic resonance (EPR) setting,[8] or via inelastic electron tunneling, i.e., within the junction of a scanning tunneling microscope (STM),[9–11] revealing also the energy spacing between the magnetic sublevels (i.e., spin-orbit splitting or magnetic anisotropy). STM affords atomic-scale spatial resolution, allowing one to address individual molecules, whereas EPR experiments require larger ensembles of magnetic units (e.g., solutions or molecular crystals). Additionally, since the electronic structure of the molecule and, consequently, its response to an applied magnetic field may change significantly by the environment due to, for example, charge transfer or polarization, it is important to verify that spin states and related spin dynamics (coherence or magnetic relaxation times) are retained upon adsorption on a surface.[12]

When grafted onto a surface or adsorbed at the apex of a scanning probe tip, molecular magnets can also serve as molecular spin probes capable of detecting states and properties of nearby nano-magnets through their magnetic interactions.[13] These interactions lead to a

shift of the spin sensor's energy levels and to a perturbation of its static and dynamic magnetic properties, which, if measured, enables sensing of the nearby magnetic species. For example, when functionalizing a metallic STM tip by such spin-probe molecules, the electrons tunneling through the molecular magnet-terminated tip can induce spin-flip transitions in magnetic molecules or arrays of molecules deposited on a support, thus addressing their spin-orbit levels, magnetic anisotropy, exchange interactions, and spin-phonon couplings.

Recently, the nickelocene molecular magnet ($NiCp_2$, Cp = cyclopentadienyl) adsorbed on metal surfaces has been investigated by STM experiments.[14–18] Due to the robustness of $NiCp_2$'s magnetic anisotropy upon adsorption and the ability to address its energy levels by STM, $NiCp_2$ has also been used to functionalize the STM's metallic tip, probing double spin-flip excitations as well as exchange interactions and coupled spin-vibration transitions in the $NiCp_2$ dimer (i.e., one $NiCp_2$ is anchored to the tip and positioned above another $NiCp_2$ deposited on a surface).[15–18] $NiCp_2$ shows robust magnetic anisotropy after adsorption on a substrate and is minimally affected by its local environment, while being strongly sensitive to the nearby magnetic molecules. Thus, to maximize the sensitivity of the spin sensor towards the desired magnetic quantity, one should be able to mitigate the undesired interactions with the surrounding.[19,20] Despite the rise of STM techniques and potential applications of $NiCp_2$ as a spin-sensing probe, microscopic understanding of the origin of $NiCp_2$ magnetic anisotropy and the resilience of its magnetic behavior is still incomplete. Furthermore, magnetic behavior of $NiCp_2$ adsorption complexes has not been yet theoretically characterized beyond DFT (density functional theory) or DFT+U (Hubbard correction to DFT). Thus, affordable yet reliable computational methods capable of investigating complex and extended model systems, such as molecular magnets on a surface or their self-assemblies, are still to be developed.[3]

Detailed understanding of electronic structure and magnetic behavior of molecular magnets is key to interpreting experiments and designing novel magnetic materials by structural modification of their building units. In the context of molecular magnets, one target quantity is the spin-reversal barrier (i.e., magnetic anisotropy), which determines the extent to which the system can be magnetized by an applied magnetic field (i.e., susceptibility) and influences the rate of magnetization switching (magnetic relaxation time), also enabling a better control over the spin states.

Ab initio description of molecular magnets' spin states is challenging because of closely ly-

ing electronic states and their multi-configurational wave functions, which are not amenable to standard single-reference treatments, such as Kohn-Sham DFT, perturbation theory (PT), and coupled-cluster (CC) methods. It is desirable to have a reliable and affordable method capable of tackling both dynamical and non-dynamical correlation in such molecular and extended systems. One strategy to treat molecular magnets entails using multi-reference (MR) methods or a broken symmetry (BS)-DFT approach, extracting magnetic anisotropy from phenomenological spin Hamiltonians.[21] Recently, we reported an alternative approach based on the equation-of-motion coupled-cluster (EOM-CC) framework, implemented in the *ezMagnet* module[22] of the *ezSpectra* suite.[23] *ezMagnet* enables extracting magnetic anisotropy (from the spin-orbit splitting) and computing macroscopic magnetic properties (magnetization and susceptibility) starting from EOM-CC calculations of magnetic states and relevant properties (SOCs and angular momentum operators). Calculated macroscopic quantities can then be directly compared with experiment, bypassing the spin-Hamiltonian formalism.

The EOM-CC family of methods[24–26] extends the hierarchy of black-box single-reference methods to strongly correlated systems. Among EOM-CC variants, the spin-flip (SF) method[27–29] provides access to multi-configurational states of polyradicals, making EOM-SF-CC suitable for applications to molecular magnets.[22,30–33] Calculations of spin-related properties also requires SOCs and Zeeman interactions (i.e., the interaction of the electrons with an applied magnetic field). *ezMagnet* treats these relativistic interactions using a two-step state-interaction scheme.[34–36] First, zero-order states are obtained from non-relativistic EOM-CC calculations. Second, in the basis of these zero-order non-relativistic EOM-CC states, a perturbed Hamiltonian is formed by including SOC and Zeeman terms. Using the EOM-CC wave functions, SOCs are computed as matrix elements of the Briet-Pauli spin-orbit Hamiltonian,[37,38] as recently implemented in the *Q-Chem* software[39,40] by Krylov and co-workers.[41–43] Then, by applying Boltzmann statistic, *ezMagnet* computes macroscopic properties from the resulting partition function, following the protocol developed by Neese and co-workers.[44]

Ideally, the theory should be able to provide not only state energies and experimental observables, but also tools for interpreting the computed properties, thus furnishing insights. In many-body correlated theories (such as EOM-CC), one can derive a molecular orbital interpretation by employing reduced quantities, i.e., one-particle transition density matrix, and corresponding natural transition orbitals (NTOs).[42,45–51] In this way, the computed

properties can be described in terms of a simple orbital picture, which is rigorously defined for many-body wave-functions and is not sensitive to the basis set or the correlation treatment, such that the comparisons between different methods can be carried out.[43,49,51,52] Within this orbital picture, hole-particle NTO pairs describe the transitions between spin-orbit coupled states,[42] so that trends in magnetic anisotropy and barrier for spin-inversion can be rationalized based on the shape of the NTO pairs contributing to the SOC,[22] and strength of exchange couplings between metal centers can be related to the frontier natural orbitals' character and occupation.[53]

In this contribution, we characterize magnetic properties of the $NiCp_2$ molecular magnet using this methodology, recently implemented in *ezMagnet* and the *Q-Chem* software,[40] in order to investigate whether $NiCp_2$'s electronic structure and magnetic behavior are sensitive to its coordination environment or not. To this end, we first consider isolated $NiCp_2$ using EOM-SF-CCSD. We then modify the local ligand field and consider six differently ring-substituted $NiCp_2$ compounds and the adsorption complex of a single $NiCp_2$ molecule on a model surface. Our set of modified nickelocene compounds includes both electron withdrawing and donating substituents as well as two bent structures, which are used as precursors of nickelocene chains. As a model surface, we consider magnesium oxide and its most commonly exposed (001) plane. Owing its well-defined ionic character and simple cubic structure, MgO is suitable for testing our approach using simplified cluster models of $NiCp_2$ on MgO(001). Insulating thin MgO layers are often used to mediate the interaction between the magnetic species and the metallic substrate, improving the magnetic bistability of the nano-magnet.[54] While EOM-CC methods (as well as other many-body approaches) scale steeply with the system size, which precludes brute-force applications to large molecular magnets, the combination of the spin-flip approach with TD-DFT (SF-TDDFT)[55,56] circumvents this problem, allowing us to investigate spin states of sufficiently large clusters of the $NiCp_2$/MgO(001) complex. Benchmark studies of Cu(II)- and Fe(III)-based molecular magnets have shown good agreement between SF-TDDFT and EOM-SF-CCSD calculations and/or experiment.[32,53] The benchmarks consistently show[32,53,56] that SF-TDDFT performs the best when deployed with the non-collinear kernel[56,57] and hybrid and range-separated hybrid functionals, such as PBE0 and LRC-ωPBEh. Another benchmark study of a set of binuclear transition-metal complexes have reported that the SF-TDDFT approach provided more accurate magnetic coupling constants (i.e., spin-state energy gaps) than BS-DFT, with

the additional advantage of avoiding the ambiguities associated with the use of non-unique spin projectors.[58]

We note that the present methodology (implemented in *ezMagnet*) for computing molecular magnetic properties is general and can be combined with any electronic structure method that can furnish SOCs and transition angular momentum. Because calculations of SOCs[41–43] and transition angular momentum are formulated using reduced density matrices, their extension to a broader class of methods is straightforward. Recent formulations of SOCs in combination with computationally more efficient than EOM-SF-CC yet reliable approaches, such as RASCI[43] and SF-TDDFT,[59] extend the scope of applicability of the algorithms implemented in *ezMagnet* to larger magnetic systems. Taking advantage of this generality, here we investigate magnetic behavior of $NiCp_2$ on MgO(001) using SF-TDDFT spin states. This is the first application of SF-based approaches to describe magnetic molecules on surfaces, illustrating the utility of this methodology. For the $NiCp_2$ molecule, we analyze the SOCs between the spin-orbit interacting states using NTOs and explain the origin of magnetic anisotropy. We then consider spin states' ordering and their orbital character as the key descriptors of the magnetic behavior of $NiCp_2$ in a modified surrounding. Preservation of such descriptors is the prerequisite for robust magnetic anisotropy against changes of the local environment, interpretation corroborated by our magnetic property calculations on the ring-substituted $NiCp_2$ compounds and on the $NiCp_2$/MgO(001) adsorption model.

The paper is organized as follows. Section II presents the theoretical background. We begin with a brief introduction of the SF approach and of the molecular orbital picture introduced to interpret the computed properties, followed by a recap of our formalism for computing SOCs, Zeeman interactions, and magnetic properties. Section III provides the computational details and describes model systems. Section IV presents the results. Our concluding remarks are given in Section V.

II. THEORETICAL BACKGROUND

We describe open-shell molecular magnets using the SF-EOM-CC method.[27–29] In SF approaches, a single-determinant high-spin state is used as a reference from which all multiconfigurational lower-spin states can be obtained by spin-flipping excitations. Within the

EOM-SF-CC formalism, target-state wave functions have the following form:

$$|\Psi\rangle^{S,S-1}_{M_S=S-1} = R_{M_S=-1}\ e^T|\Phi_0\rangle^S_{M_S=S}, \tag{1}$$

where $|\Phi_0\rangle$ is the high-spin reference Slater determinant, $e^T|\Phi_0\rangle$ is the CC wave function, and R is an excitation operator that flips the spin of an electron. EOM-SF provides a balanced treatment of relevant spin states, does not require choosing an active space, and describes dynamical and non-dynamical correlation in a single computational step. EOM-SF has been successfully used to treat ground and excited states of various molecular magnets.[22,30–33] We describe singlet and triplet states of $NiCp_2$ and of the six ring-substituted $NiCp_2$ derivatives by EOM-SF-CCSD starting from a high-spin d^8 triplet reference. To describe the $NiCp_2$/MgO(001) model complex, we use SF within the TD-DFT ansatz.[55,56]

Magnetic properties arise from spin-orbit and magnetic field (Zeeman) interactions. We describe these effects by a two-step state-interaction procedure:[22] first, EOM-CC states are computed and then these states are used to evaluate matrix elements of the spin-orbit (H^{SO}) and Zeeman (H^{Z}) operators. The latter describes the interaction of the electrons with the external magnetic field $\mathbf{H}$

$$H^{\mathrm{Z}} = \mu_B \mathbf{H}\left(\mathbf{L} + g_e\mathbf{S}\right), \tag{2}$$

where $g_e = 2.0023$ is the free spin g-factor, μ_B is the Bohr magneton, and $\mathbf{S}$ and $\mathbf{L}$ are the total spin and orbital angular momentum operators, respectively. Spin-orbit interactions are treated by using the Breit-Pauli Hamiltonian.[37,38] Spin-orbit and field-perturbed states are then obtained by diagonalization of the zero-order Hamiltonian (H^0) augmented by H^{SO} and H^{Z}:

$$H = H^0 + H^{\mathrm{SO}} + H^{\mathrm{Z}}. \tag{3}$$

In *Q-Chem*,[40] calculation of SOCs and matrix elements of the Zeeman operator is currently implemented for EOM-SF-CC, RASCI, and SF-TDDFT,[41,43,59] and can be easily extended to any method that can provide reduced density matrices.

To gain insight into the nature of electronic states and transitions, we analyze magnetic behavior of $NiCp_2$ using transition density matrix between spin-orbit interacting states and the resulting NTOs. In previous studies, such analysis has been carried out for diradical and iron-based molecular magnets, whose SOCs are determined by one NTO contribution only.

Here, we extend this treatment to the cases in which two leading NTO pairs contribute to the transition property.

The key quantity is the one-electron transition density matrix:

$$\gamma_{pq}^{FI} = \langle \Psi^F | a_p^\dagger a_q | \Psi^I \rangle, \tag{4}$$

where $a_p^\dagger$ and a_q are the creation and annihilation operators associated with the ϕ_p and ϕ_q molecular orbital basis. A singular-value decomposition[60,61] of γ_{pq}^{FI} yields the most compact description of the one-electron excitation in terms of a unique set of orbitals — hole and particle NTOs — which are independent of the method/basis set choice thus allowing a meaningful comparison of different levels of theory. In the basis of these NTOs, expectation values of one-electron operators ($\hat{A}$) can be computed as:

$$\langle \Psi^F | \hat{A} | \Psi^I \rangle = \sum_{k,l} \sigma_k \sigma_l \langle \psi_k^p | \hat{A} | \psi_l^h \rangle, \tag{5}$$

where σ are singular values associated to the NTO pairs. Except for the trivial case of one dominant NTO pair, observables can be affected from the contribution of cross terms, which may lead to very different properties for transitions between states characterized by equivalent NTO pairs.[50,62,63] Here, we show that nickelocene's states with identical NTOs can have very different SOC based on the different form of their two-configurational wave function (symmetric or antisymmetric combination, see discussion in Section IV and in Section 5 of the Supplementary Information (SI).

SOC is responsible for the zero-field splitting of the $2S+1$ degenerate components of the spin S ground state, giving rise to spin-inversion barrier ($U = |D| \cdot S^2$) and magnetic anisotropy (quantified by the spin-Hamiltonian parameter D). Temperature- and field-dependent magnetization and susceptibility are obtained from first- and second-order derivatives, respectively, of the resulting partition function ($Z = \sum_n e^{-E_n(\mathbf{H})/RT}$) with respect to the field,[44]

$$\mathbf{M}(T, \mathbf{H}) = NkT \frac{\partial ln Z(T, \mathbf{H})}{\partial \mathbf{H}} \tag{6}$$

and

$$\chi(T, \mathbf{H}) = NkT \frac{\partial^2 ln Z(T, \mathbf{H})}{\partial \mathbf{H}^2}, \tag{7}$$

which allows direct comparison with experiment without relying on the spin-Hamiltonian formalism. In Eqs. (6) and (7), $\mathbf{H}$ is the magnetic field vector, while $E_n(\mathbf{H})$ are the SOC- and field-perturbed energies of the magnetic sublevels contributing to the partition function $Z(T, \mathbf{H})$. This computational approach is implemented in the *ezMagnet* software and was shown to yield accurate results for a set of small- and medium-sized iron-based SMMs.[22] This approach is general and can be combined with any other *ab initio* method, which provides angular momentum and spin-orbit matrix elements, e.g., SF-TDDFT and RASCI for more extended systems. Calculation of matrix elements of the spin operator entering Eq. (2) can be easily derived from spin S and spin projection M_S of the states involved.[22]

III. COMPUTATIONAL DETAILS AND MODEL SYSTEMS

To investigate the origin of magnetic anisotropy in the nickelocene ($NiCp_2$) molecular magnet, we first consider an isolated $NiCp_2$ molecule. In $NiCp_2$, the Ni(II) transition metal ion is sandwiched between two cyclopentadienyl (Cp or $C_5H_5^-$) rings. $NiCp_2$ has a triplet ground state with a d^8 electronic configuration. The molecule possesses a C_5 rotational axis collinear with the z direction. Here, we consider the centrosymmetric staggered molecular structure (ligand field of D_{5d} symmetry) with mean Ni–C distance of 2.185 Å, taken from single-crystal X-ray diffraction studies.[64] Magnetic susceptibility measurements revealed a deviation from the Curie-Weiss law below 70 K.[65,66] This departure from the Curie isotropic behavior of a paramagnetic molecule has to be ascribed to the large SOC and, thus, ZFS of the magnetic sublevels (with $M_S = \pm 1, 0$) of the triplet ground state. Fig. 1 shows $NiCp_2$ staggered configuration, electronic states (both triplet and singlet), and spin-orbit splitting of the triplet ground state as computed from EOM-SF-CCSD calculations.

We also examine ligand-field effects on $NiCp_2$ electronic structure (e.g., spin state ordering and energy gaps) and magnetic behavior (e.g., magnitude of SOCs) and select a series of six differently ring-substituted $NiCp_2$ derivatives. Below we refer to the individual molecules by the numbers shown in Fig. 2. In complex 1, one C–H group for each $C_5H_5^-$ ring is replaced by a phosphorus atom, following the strategy adopted in the design of bis-cyclopentadienyl dysprosium molecular magnets to enhance spin-reversal energy barrier and operating temperature.[67,68] We then examine three systems in which one hydrogen atom for each Cp framework is substituted by an isovalent functional group: complex 2 includes two

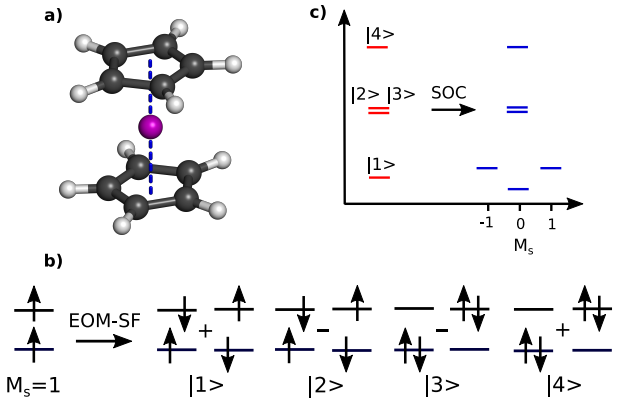

FIG. 1: a) Structures of the nickelocene with staggered rings (coordinates are from Ref. 64). Color code: Ni — purple, C — gray, and H — white. b) Electronic configurations of the high-spin $M_S = 1$ triplet reference and the low-spin target states: $M_S = 0$ triplet ($|1\rangle$) and singlets ($|2\rangle$, $|3\rangle$, and $|4\rangle$). State energies and character are obtained from EOM-SF-CCSD calculations. c) Four lowest electronic states and spin-orbit splitting of the $S = 1$ ground state. Spin-orbit splitting is computed via a two-step state-interaction scheme.

methyl groups, complex 3 has two cyano groups, and complex 6 includes two aromatic ring substituents. Preparation of complex 2, i.e., $Ni(C_5H_4R)_2$ with R = CH_3, is reported in Refs. 69,70. Complex 4 is selected as precursor of $NiCp_2$-based chains to be used as memory devices.[71] Complex 5 is an example of bridged $NiCp_2$ in which the two Cp units are linked by naphthalene.[72] Structures of complex 1, 2, 3, and 6 were optimized with ωB97X-D/cc-pVDZ for the high-spin triplet state, whereas for complex 4 and 5, experimental bent structures were considered, as reported in Ref. 71 and Ref. 72, respectively.

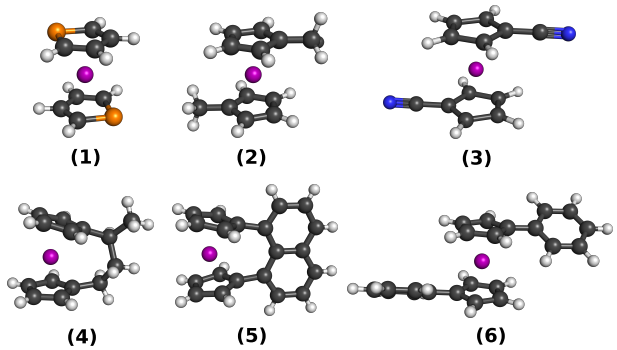

FIG. 2: Structures of six ring-substituted nickelocene derivatives. In complex 1 two C–H groups are substituted with two P atoms. In complex 2, 3, and 6, two H atoms are substituted with methyl, cyano, and aromatic groups, respectively. Complexes 4 and 5 are bent structures taken from Ref. 71 and Ref. 72, respectively. Color code: Ni — purple, P — orange, N — blue, C — gray, and H — white.

We also investigate electronic structure and magnetic behavior of $NiCp_2$ adsorbed on a

support using MgO(001) as a model surface. MgO is chosen due to its insulating character and low phonon density, thereby suppressing magnetic relaxation via negligible spin-phonon coupling.[73] To obtain a reliable finite-cluster model of $NiCp_2$ on the MgO(001) surface, we used an embedded cluster approach, which is often employed in computational catalysis to describe isolated point defects or isolated adsorbed molecules on ionic surfaces.[74] This structural model is well suited for the description of individual molecular magnets on a surface, whereas using periodic boundary conditions would require large supercell to minimize the artificial molecule-molecule interactions with the periodic images. Further details can be found in Section 6 of the SI.

First, we performed a DFT structure optimization of the $NiCp_2/Mg_{49}O_{49}$ model cluster embedded in a sufficiently large array of point charges resembling the ionic MgO surface. Fig. 3 shows our embedded cluster model. We increase the number of point charges to converge adsorption energy and equilibrium distance between the $NiCp_2$ and MgO(001) surface (see Table S7 in the SI). Second, we considered a smaller cut-out (i.e., $NiCp_2/Mg_{25}O_{25}$) of the optimized $NiCp_2/Mg_{49}O_{49}$ model cluster and investigate spin states and magnetic properties of $NiCp_2$ on MgO(001) using the SF-TDDFT ansatz. For DFT structure optimizations, we employed the PBE0[75,76] functional, whereas to compute spin states, we followed recommendations in Refs. 32,53 for transition-metal compounds and used SF-PBE0 and SF-LRC-ωPBEh[77] within the non-collinear formulation of SF-TDDFT.[56,57] The size and shape of the $NiCp_2/Mg_{25}O_{25}$ quantum mechanical region was chosen to minimize the computational cost while providing a structural model comparable with models already available in the literature for adsorbates on MgO(001).[78,79] STM images of $NiCp_2$ on Cu(001)[14–16] and Ag(110)[17,18] show that $NiCp_2$ is bonded perpendicularly to the surface through a Cp ring, whereas the other Cp ring is exposed to the vacuum. For these reasons, we take inspiration from previous studies on metal substrates[14–18] and select the $NiCp_2$ perpendicularly adsorbed on MgO(001) as guess structure. Additionally, we investigate two possible adsorption sites, i.e., Ni(II) ion on top of oxygen and magnesium.

For $NiCp_2$ and its six derivatives, triplet ground states and singlet excited states are computed using EOM-SF-CCSD, whereas for the model complex of $NiCp_2$ on MgO(001) we employed SF-TDDFT. All SF calculations are performed starting from a high-spin triplet state, as shown in Fig. 1. This reference state is represented by a single determinant (high-spin $M_S = 1$) and is well described by the CC expansion of the wave function or by

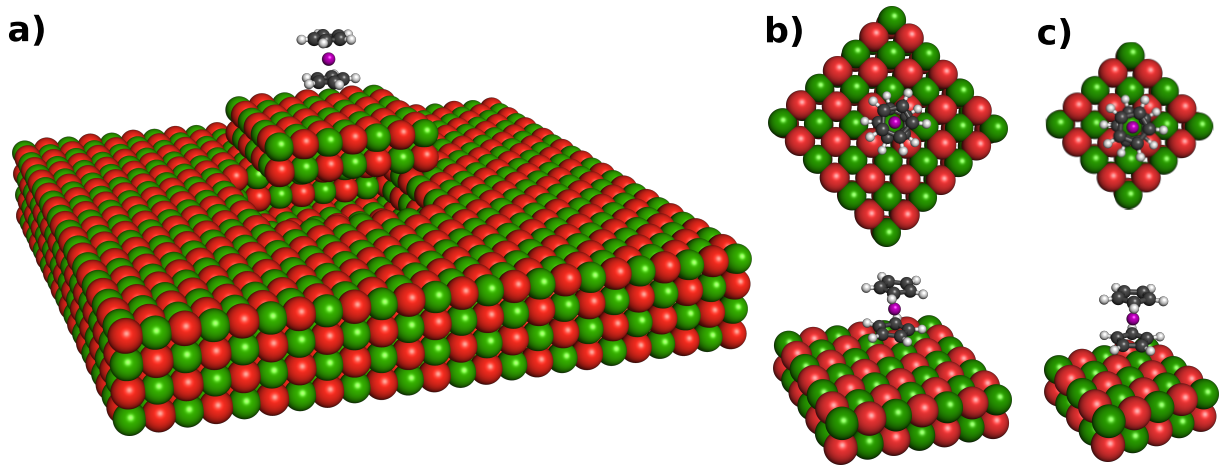

FIG. 3: a) The embedded cluster setup used for structure optimization: the all-electron QM region ($NiCp_2/Mg_{49}O_{49}$) is treated with PBE0/6-31G*, while the outermost region contains point charges. The QM region is shown as lifted for clarity. Here, $NiCp_2$ is on-top of Mg^{2+} adsorption site. b) Top and side views of the embedded $NiCp_2/Mg_{49}O_{49}$ PBE0 region. c) Top and side views of a smaller cut-out ($NiCp_2/Mg_{25}O_{25}$) used for the SF-TDDFT calculations. Color code: Ni — purple, Mg — green, O — red, C — gray, and H — white.

Kohn-Sham DFT. From this reference, single SF excitations generate the triplet state linear combination of two $M_S = 0$ determinants with equal weights and three singlet states of open-shell character. Given that $NiCp_2$ compounds have a triplet $S = 1$ ground state, the energy barriers for spin inversion $U = |D| \cdot S^2$ is equal to the magnetic anisotropy D.

For isolated $NiCp_2$ and complexes 1-4, we used Dunning's cc-pVTZ basis set.[80–82] The SOC calculations of complexes 5 and 6 and of $NiCp_2/Mg_{25}O_{25}$ adsorption complex were performed using Dunning's cc-pVDZ basis set.[80–82] As noted before,[22] using cc-pVTZ rather than cc-pVDZ has a negligible effect on the state energy, magnetic anisotropy, and computed magnetization and susceptibility data (deviations are less than 1 cm^{-1} for D and within 1% for the average magnetization and susceptibility, see Tables S3 and S4 and Fig. S6 in Section 2 of the SI). For isolated $NiCp_2$, SF-PBE0 reproduces well state ordering, magnetic anisotropy, and magnetic properties as compared with EOM-SF-CCSD (Section 2 of the SI), but the relative energies are quite different (e.g., triplet-singlet energy gap is about 9800 cm^{-1} for EOM-SF-CCSD and 6500 cm^{-1} for SF-PBE0).

Importantly, the calculated SOCs of isolated $NiCp_2$ is not sensitive to the basis set quality (cc-pVDZ or cc-pVTZ) neither to the *ab initio* method adopted (EOM-SF-CCSD or SF-PBE0), see Table S10.

Open-shell reference states were treated using unrestricted Hartree-Fock (HF). For $NiCp_2$,

spin contamination of the reference and EOM-SF-CCSD states is small: the corresponding $\langle S^2 \rangle$ values are 2.00 for $S = 1$ and between 0.06 and 0.13 for the singlet states (see Table S1 in the SI). For the six ring-substituted $NiCp_2$ compounds, spin contamination is less than 0.23, whereas, for the $NiCp_2$/MgO model complex, deviations are less than 0.08, see Table S2 and S8 in the SI.

To speed up the EOM-SF-CCSD calculations, we applied: (i) Frozen-core approximation; (ii) Cholesky decomposition[83] with a threshold of 10^{-3} for two-electron integral calculations, (iii) open-shell frozen natural orbital (OSFNO)[84] truncation of the virtual space with the total population threshold of 99%, and (iv) single precision execution.[85]

All electronic structure calculations were performed using the Q-Chem software.[39,40]

IV. RESULTS AND DISCUSSION

For isolated $NiCp_2$, we computed four spin states: a triplet ground state and three singlet excited states (see Fig. 1). The effective number of unpaired electrons,[86] $n_{n,nl}$, of each state is exactly 2, indicative of a strong diradical and open-shell character (see Table S1 in the SI). Fig. S1 shows frontier natural orbitals for the four states. These are nearly perfect d_{xz} and d_{yz} orbitals, indicating that unpaired electrons are mainly localized on the Ni(II) metal center, with almost no involvement of the Cp rings. For each transition between the spin-orbit coupled states, two NTO pairs contribute to the overall SOC (the number of non-zero singular values is about 2). Fig. 4 shows the two leading NTO pairs between states 1 and 2. Transition between states 1 and 2 involve an orbital torque from d_{yz} to d_{xz} (first NTO pair) and vice versa (second NTO pair). Similar picture describes the transition between the triplet ground state and higher singlet excited states (see Figs. S2 and S3 in the SI).

The SOC between the triplet ground state and the singlet excited states lifts the degeneracy of the $NiCp_2$ triplet ground state, which results in a low-spin ($S = 1$, $M_S = 0$) ground state and a high-spin ($S = 1$, $M_S = \pm 1$) doubly degenerate excited state (see Fig. 1). The energy barrier between the ground state and the first excited state is about 15 cm^{-1}. Due to the axial symmetry of $NiCp_2$ and to the spin $S = 1$ character of its ground state, this energy barrier corresponds to the axial magnetic anisotropy (D). The computed value of $D = 15$ cm^{-1} agrees reasonably well with the experimentally derived D parameter, which ranges between 25.6[65] and 33.6[66] cm^{-1}, and with the NEVPT2/def2-TZVP value of 40 cm^{-1}.[87] Our

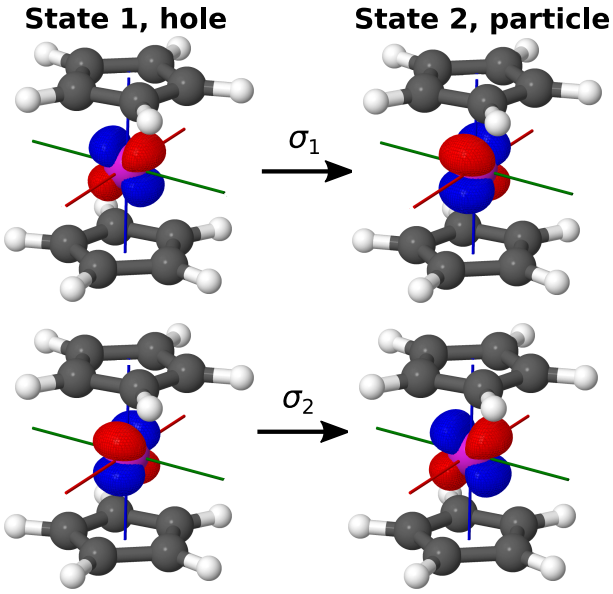

FIG. 4: Hole and particle NTO pairs of the spinless density matrix, giving rise to SOC within the states 1 and 2 of nickelocene (EOM-SF-CCSD/cc-pVTZ). Singular values σ are 1.19 and 1.15, respectively. Red, green, and blue axes indicate x, y, and z coordinates axes, respectively.

calculations confirm that D is positive, which implies that magnetic sublevel ordering is inverted with respect to molecules with negative D values, such as single-molecule magnets. The latter have the states with highest spin projection ($M_S = \pm S$) that are degenerate and lowest in energy, while for $NiCp_2$ the doubly degenerate level with spin projection $M_S = \pm 1$ is the first excited state.

Fig. 5 shows the computed magnetization M for a field oriented parallel and perpendicular to the C_5 rotational axis; powder magnetization (M_{av}) is obtained by numerical averaging over a large set of field orientations. The magnetization curves rise with the field strength, but do not saturate at strong magnetic fields. Fig. 5 shows the temperature dependence of the computes susceptibility main values (i.e., χ_{X_m}, χ_{Y_m}, χ_{Z_m}) obtained by diagonalization of the susceptibility 2nd-rank tensor. $\chi_{Z_m}T$ and $\chi_{X_m}T$ go to zero when T approaches zero; $\chi_{Z_m}T$ continuously decreases, while $\chi_{X_m}T$ passes through a maximum. We note that these field- and temperature-dependencies of the magnetization and susceptibility are fingerprints for any spin-triplet molecule with positive axial zero-field splitting D.[88] The measured temperature dependence of the inverse of the susceptibility (black and green curves in Fig. 6) shows that beyond 70 K results follow the Curie-Weiss law, i.e., $\chi = C/(T - \Theta)$, where C is the Curie constant and Θ is the Weiss constant.[65,66] Below 70 K, however, a deviation from this law is observed.[65,66] In agreement with experiments, the computed χT value at 298 K

is close to the expected value of 1.0 cm^3K/mol for a spin-only $S = 1$ system that follows the Curie law (see Section 3 in the SI), and predict a deviation from linearity (Curie law) at low temperatures (red curve in Fig. 6).

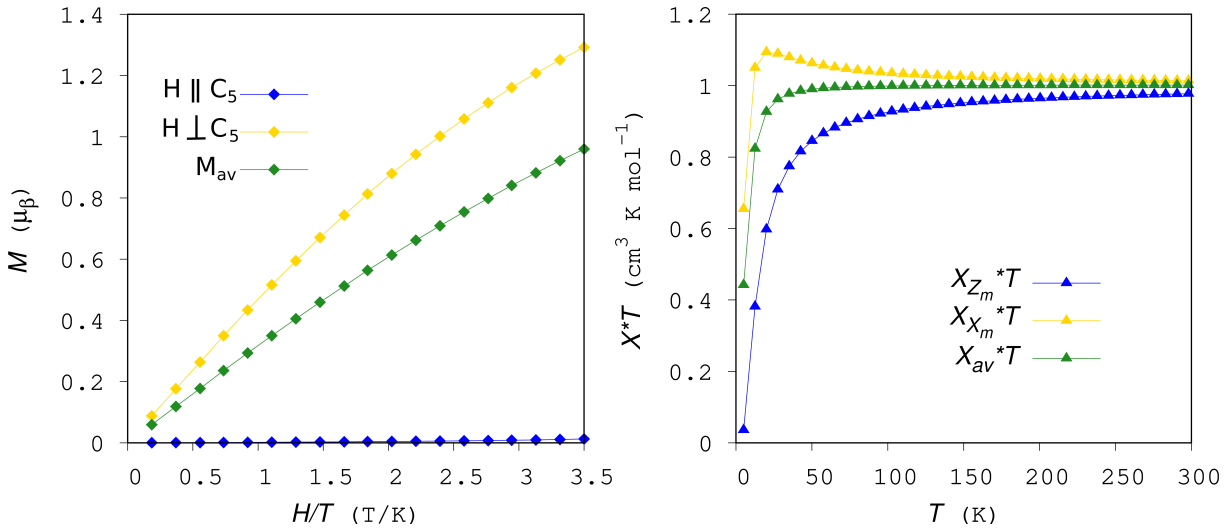

FIG. 5: Calculated field-dependent magnetizations (on the left) of $NiCp_2$ at low temperature ($T = 2$ K). Magnetization is in Bohr magneton (μ_b) units. Calculated $\chi_{Z_m}T$, $\chi_{X_m}T$ ($\chi_{Y_m}T$), and $\chi_{\rm av}T$ (on the right) of $NiCp_2$ in the temperature range from 5 to 300 K and under an applied field of 1 T. "av" stands for isotropic powder averaging.

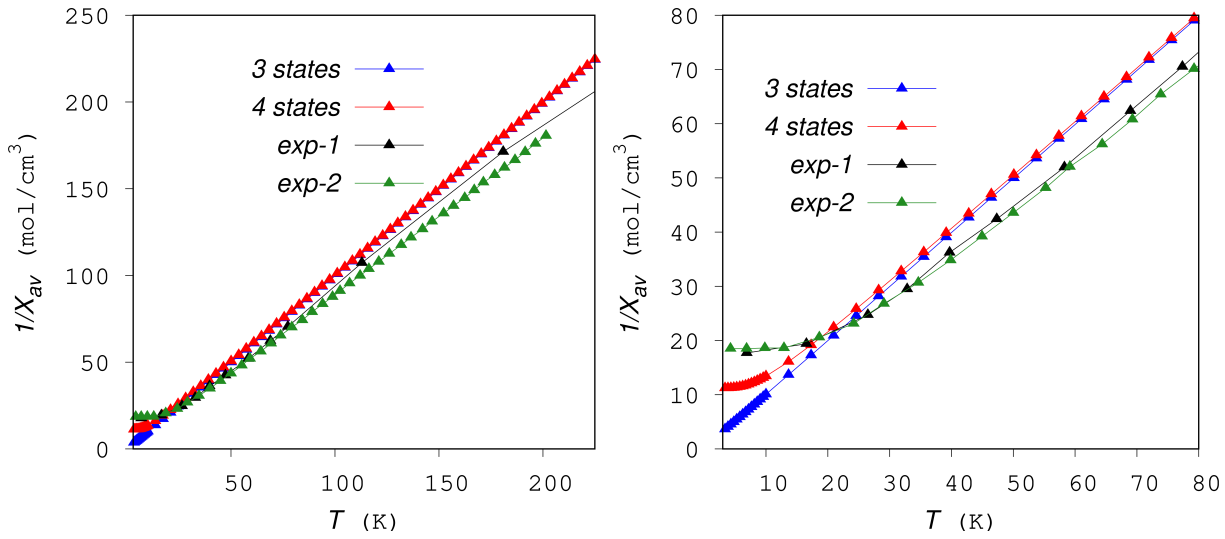

FIG. 6: Calculated temperature dependence of the inverse susceptibility ($1/\chi_{\rm av}$) of $NiCp_2$ in the temperature range from 5 to 250 K (on the left) and from 5 to 80 K (on the right), and under an applied field of 1 T. Calculated curves including three and four electronic states are in blue and red, respectively. Experimental susceptibility data, i.e. black and green curves, are taken from Ref. 65 and Ref. 66, respectively.

To explain the nature of this magnetic behavior, we combine the NTO-picture of Fig. 4

(as well as of Figs. S2 and S3) and the transition-density matrix based analysis of calculated orbital angular-momentum matrix elements and SOCs of Table S6 with their explicit calculation using wave functions of triplet and singlet states for a two-electron in two-orbital system of Section 5 of the SI. Table S6 reports $\langle L_i \rangle$ with $i = x, y, z$ and SOC matrix elements. Orbital angular momentum between state 1 and states 2, 3, and 4 is zero. However, while the calculated SOC is small between states 1 and 2 and states 1 and 3, SOC is large between states 1 and 4, which is the origin of the anisotropic magnetic behavior of $NiCp_2$ and deviation from the Curie law at low temperatures. We note that for the transition between states 1 and 4, it is the average value $\langle \hat{H}^{SO}_{L_i} \rangle$ of the $\hat{H}^{SO}_{L_z}$ component of the spin-orbit operator to be large, while $\langle \hat{H}^{SO}_{L_x} \rangle$ and $\langle \hat{H}^{SO}_{L_y} \rangle$ values are small. Indeed, if the spin-orbit interaction between state 1 and the higher in energy singlet excited state (state 4) is not included, the calculations fail to reproduce the experimental trend at low temperatures (see blue curve in Fig. 6). This can be explained by looking at the eigenvalue analysis of the transition density matrix. Each NTO pair contributes with the same weight to the overall SOC. However, while for states 1 and 2 and for states 1 and 3, the sign of the two leading NTO contributions is opposite, leading to the SOC cancellation, for states 1 and 4, the sign of the two SOC contributions is the same, giving rise to large SOC. El-Sayed's rules[89] explain why the cross terms in Eq. (5), i.e., $\langle d_{xz} | \hat{H}^{SO}_{L_z} | d_{xz} \rangle$ and $\langle d_{yz} | \hat{H}^{SO}_{L_z} | d_{yz} \rangle$, are zero because of no orbital torque in between. This can be rationalized by considering the proportionality between the spin-orbit $\hat{H}^{SO}_{L_z}$ and orbital angular momentum L_z operators, and that, in the basis of real harmonics (d orbitals in the case of $L = 2$), average values $\langle L_z \rangle$, thus $\langle \hat{H}^{SO}_{L_z} \rangle$, are zero between two identical d orbitals. In addition, by knowing triplet and singlet wave functions of $NiCp_2$ (i.e., two electrons localized in two orbitals ϕ_A and ϕ_B), one can explicitly compute transition orbital momentum and SOC between the $S = 1$ ground state and the three $S = 0$ excited states (see Section 5 of the SI). The computed orbital angular momentum between states 1 and states 2, 3, and 4 is zero because of their different spin (triplet versus singlet), consistent with the results in Table S6 obtained from *ab initio* calculations. In contrast, we obtain a zero $\langle 1 | H^{SO} | 2 \rangle$ and $\langle 1 | H^{SO} | 3 \rangle$ SOC, while SOC between states 1 and 4 is large, as predicted by the full calculation of the SOC matrix elements (see Table S6). This result can be ascribed to the different nature of the wave functions of the three

singlet states:

$$|2\rangle \sim (\phi_A(1)\phi_B(2) + \phi_B(1)\phi_A(2))(\alpha(1)\beta(2) - \beta(1)\alpha(2)) \quad (8)$$

$$|3\rangle \sim (\phi_A(1)\phi_A(2) - \phi_B(1)\phi_B(2))(\alpha(1)\beta(2) - \beta(1)\alpha(2)) \quad (9)$$

$$|4\rangle \sim (\phi_A(1)\phi_A(2) + \phi_B(1)\phi_B(2))(\alpha(1)\beta(2) - \beta(1)\alpha(2)). \quad (10)$$

Wave functions $|2\rangle$, $|3\rangle$, and $|4\rangle$ share the same spin part. Wave functions $|3\rangle$ and $|4\rangle$ have similar spatial component except for a sign: in state $|4\rangle$ the two configurations appear with the same sign, while in state $|3\rangle$ they appear with the opposite sign. Spatial component of wave function $|2\rangle$ is different. Due to the common spin component of these wave functions, for all spin-orbit couplings, only $\langle m|L_zS_z|n\rangle$ term of the spin-orbit operator (i.e., $H^{SO} \approx L_+S_- + L_-S_+ + L_zS_z$) can survive due to a non-zero $\langle S_z\rangle$ contribution. However, due to the same sign in the spatial part of wave function $|4\rangle$, only $\langle 1|L_zS_z|4\rangle$ and thus $\langle 1|H^{SO}|4\rangle$ is large because of a non-zero $\langle L_z\rangle$ term, while $\langle L_z\rangle$ terms between states 1 and 2 and states 1 and 3 vanish, and so does the SOC.

We also consider six differently substituted $NiCp_2$ molecules (Fig. 2), with the goal to investigate weather changes in the local ligand fields (i.e., electron withdrawing/donating substituents or bent structures) influence the triplet-singlet energy gap and so the SOC affecting their magnetic behavior. Equilibrium structure of nickelocene does not change significantly upon substitution of hydrogen atoms with methyl, cyano, and aryl groups (Ni–Cp ring height is about 1.82 Å). After integration of P, the P–C distance increases from the average value of 1.38 (for C–C bond) to 1.78 Å, but the sandwich structure is retained. Therefore, nickelocene structure is resistant against ring substitution. Moreover, our calculation show that all substituted $NiCp_2$ molecules preserve the same spin state ordering (Table S2) and orbital character (Figs. S4 and S5). Additionally, also the spin-orbit splitting (quantified by the energy barrier U or by the parameter D in Table S2) and the anisotropic magnetic behavior (Fig. 7) do not change. This confirms that magnetic anisotropy of $NiCp_2$ is not affected by changes of the ligand field.

If one desires to use $NiCp_2$ molecular magnets to trigger spin-flip transitions in magnetic molecules, atoms, or arrays of magnetic unit on a support, it is important to verify whether $NiCp_2$ magnetic behavior is affected by the interactions with the support. If not, any change in the spin excitation spectrum of nickelocene would reflect electronic structure and

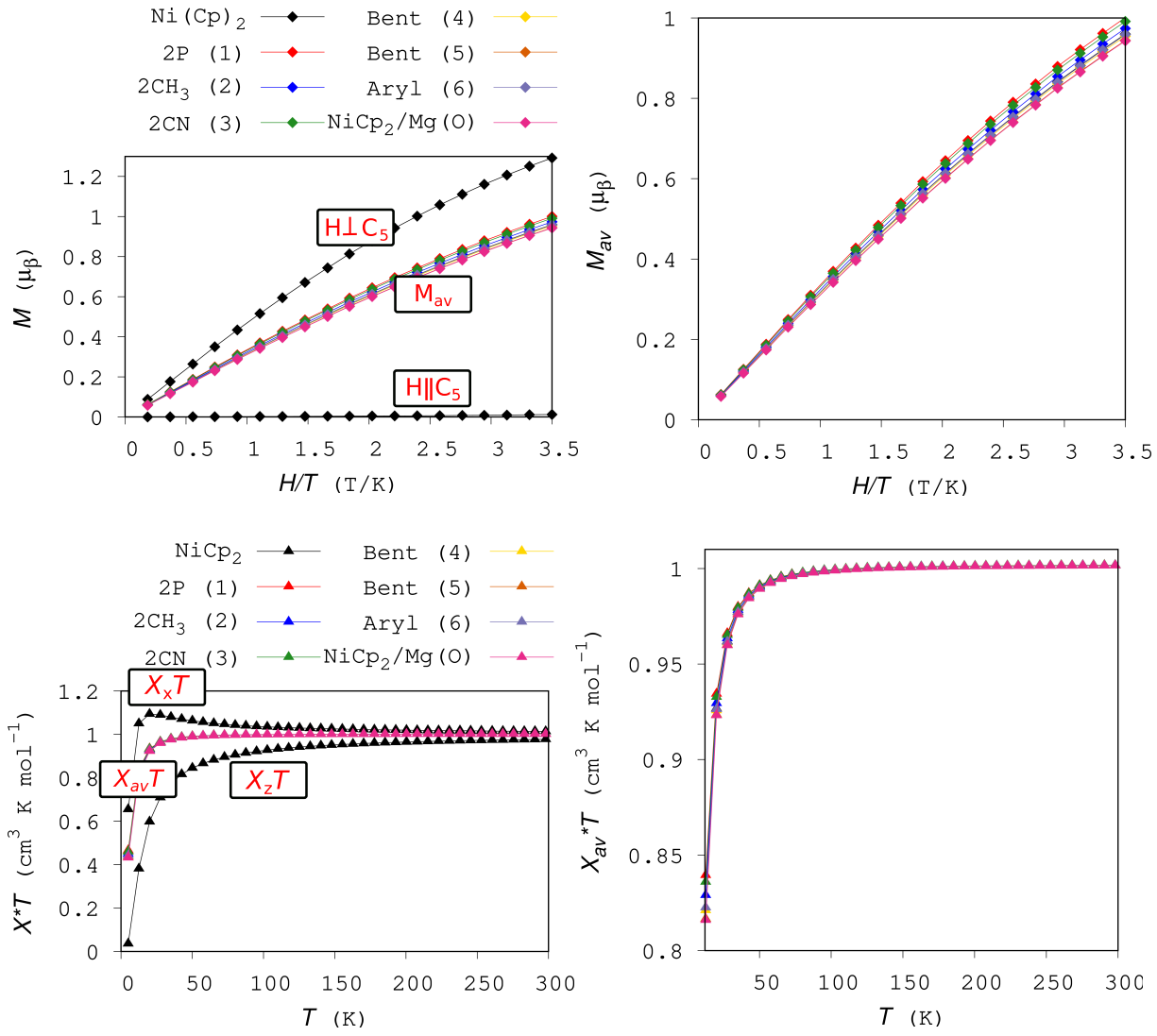

FIG. 7: Calculated field-dependent magnetizations (top) of (i) $NiCp_2$, (ii) six ring-substituted $NiCp_2$ compounds, and (iii) $NiCp_2/Mg_{25}O_{25}$ adsorption complex (T = 2 K). Magnetization is in Bohr magneton (μ_b) units. Calculated $\chi_{Z_m}T$, $\chi_{X_m}T$ ($\chi_{Y_m}T$), and $\chi_{\rm av}T$ (bottom) in the temperature range from 5 to 300 K and under an applied field of 1 T. "av" stands for isotropic powder averaging. Properties are obtained by EOM-SF-CCSD/cc-pVTZ calculations, with the exception of complexes 5 and 6 for which we employed EOM-SF-CCSD/cc-pVDZ and of $NiCp_2/Mg_{25}O_{25}$ for which we used SF-PBE0/cc-pVDZ.

magnetic properties of the magnetic molecule in the proximity, and $NiCp_2$ could be used a spin sensor. To verify this assumption, we consider $NiCp_2$ adsorbed on a model surface (i.e., MgO(001)) and investigate its chemical and electronic structure. From the DFT structure optimizations of $NiCp_2$/MgO(001), we identified the O-top as the most favorable adsorption site (see Table S7 in the SI). $NiCp_2$ does not deform upon adsorption. The staggered configuration of $NiCp_2$ is retained and $NiCp_2$ is found to adsorb perpendicularly to the

surface through one Cp ring, similarly to $NiCp_2$ on metal substrates.[14–18] The Ni–Cp ring height decreases from 1.82 to 1.78 Å upon adsorption on MgO(001), which corresponds to a small charge transfer from the molecule to the surface. The adsorption energy is small (about -7 kcal/mol), indicative of physisorption. Fig. S10 in the SI shows the spin density for the isolated $NiCp_2$ and for the $NiCp_2$/MgO model cluster. For $NiCp_2$, spin density is localized on the frontier d_{xz} and d_{yz} orbitals of the Ni atom. Upon adsorption, spin density is preserved; the molecule retains S=1 and there is no significant spin polarization from the surface. Table I compares electronic states of isolated $NiCp_2$ with its electronic structure on the MgO(001) surface. Whereas electronic states of the isolated molecule are computed with EOM-SF-CCSD, EOM-SF-MP2 and SF-TDDFT, the electronic states of the adsorption complex are accessible by SF-TDDFT only. Table S8 shows full comparison. We observe that the relative energies depend significantly on the electronic structure method, however, the spin-state ordering and orbital character of the states for $NiCp_2$ on MgO(001) are unchanged. Moreover, similarly to the isolated molecule, Fig. 8 shows that the two leading NTO pairs between triplet and singlet states of $NiCp_2$ on MgO involve an orbital rotation between d_{xz} and d_{yz} orbitals. This analysis indicates that magnetic anisotropy and magnetic properties of $NiCp_2$ on MgO(001) would also be retained, which is confirmed by our magnetic properties calculations (see magnetization and susceptibility plots of Fig. 7 and magnetic anisotropy of Table S9). Our calculations also reveal that SOC and related spin-orbit splitting (i.e., D) of the molecule are not sensitive to the adsorption on the model MgO(001) surface (see Table S9 and S10). These results for $NiCp_2$/MgO(001) are consistent with previous STM studies investigating the adsorption of $NiCp_2$ on a metal surface.[15–18] When placed above a Cu(001)[15] (or Ag(110))[17] surface, a magnetic anisotropy energy D of 26 cm^{-1} (or 31 cm^{-1}) was determined by STM experiments, which is consistent with experimental D values for $NiCp_2$ powder samples (25.6[65] and 33.6[66] cm^{-1}), and with our results for the isolated $NiCp_2$ and the $NiCp_2$/MgO(001) adsorption complex.

Our results indicate that $NiCp_2$ is extremely robust against perturbations of its ligand field (by modifying substituents) and of its local environment (by adsorption on a metal[15–18] or insulating surface as investigated in this work), which is key property for molecular spin sensors capable of targeting magnetic interactions in the proximity rather than modification of its surrounding.

TABLE I: Energies (in cm^{-1}) of the four lowest states of the isolated $NiCp_2$ and of $NiCp_2$ on top of MgO(001), computed using EOM-SF-CCSD/cc-pVTZ and SF-TDDFT/cc-pVTZ with PBE0. "$NiCp_2$/(Mg)O" and "$NiCp_2$/Mg(O)" stand for the adsorption complexes of $NiCp_2$/MgO(001) with the Ni atom on-top of Mg^{2+} and O^{2-} adsorption sites, respectively (cluster model: $NiCp_2/Mg_{25}O_{25}$). Differences between $NiCp_2$ and $NiCp_2$/MgO with SF-PBE0 are reported in parenthesis.

	$NiCp_2$		$NiCp_2$/(Mg)O	$NiCp_2$/Mg(O)
	EOM-SF-CCSD	SF-PBE0	SF-PBE0	SF-PBE0
$\|1\rangle$	0.0	0.0	0.0	0.0
$\|2\rangle$	9805.5	6552.1	6438.1 (144.0)	6434.4 (117.4)
$\|3\rangle$	9894.2	6585.6	6450.7 (134.9)	6464.8 (120.7)
$\|4\rangle$	15144.0	12240.5	12052.9 (187.6)	12041.1 (199.4)

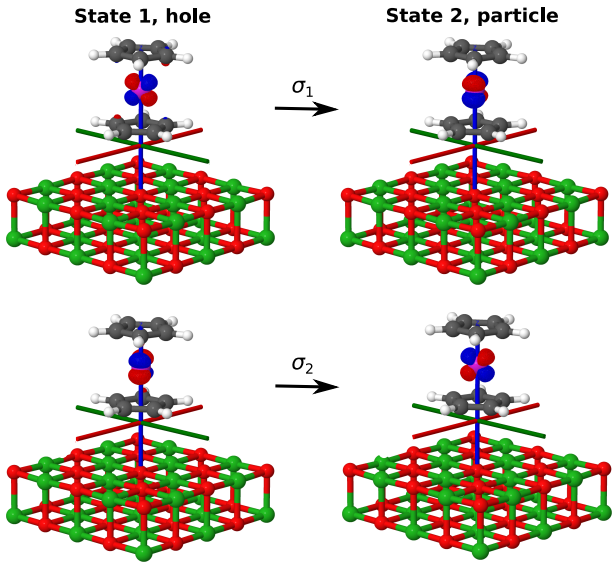

FIG. 8: Hole and particle NTO pairs of the spinless density matrix between states 1 and 2 of the $NiCp_2/Mg_{25}O_{25}$ adsorption complex (SF-PBE0/cc-pVTZ). Ni atom is on-top of O^{2-}. Singular values σ are 0.5 and 0.5, respectively. Red, green, and blue axes indicate x, y, and z coordinates axes, respectively.

V. CONCLUSION

We investigated electronic structure and magnetic behavior of the $NiCp_2$ molecular magnet and of its derivatives (i.e., six ring-substituted $NiCp_2$ and the $NiCp_2$/MgO adsorption model) using EOM-SF in combination with the *ezMagnet* software.

For the isolated $NiCp_2$, calculated magnetic anisotropy and susceptibility curves agree well with experiment, reproducing the deviation from the Curie law in the low temperature regime. We demonstrated that such anisotropic magnetic behavior originates from the SOC

between the triplet ground state (state 1) and the third singlet state (state 4), which is large, while coupling with lower singlet states (states 2 and 3) is small and does not affect $NiCp_2$'s magnetic behavior. Although $NiCp_2$ singlet excited states are characterized by two nearly equivalent NTO transitions (same nature and same weight), the NTO contributions to the SOC are canceling out between states 1 and 2 (or 3), while for the highest in energy singlet state, the NTO contributions have same sign and sum up, leading to a substantial SOC. This analysis of the SOCs is then combined with explicit calculation of SOCs using wave functions of triplet and singlet states for a two-electron in two-orbital system. By doing so, we found that SOC between states 1 and 4 survives because of the nature of the singlet wave function of state 4, i.e., symmetric combination of two Slater determinants, while it vanishes between states 1 and 2 (or 3), whose wave functions are characterized by an antisymmetric combination of two leading configurations.

Upon modification of $NiCp_2$ ligand field and adsorption of $NiCp_2$ on the MgO(001) surface model, we observed that $NiCp_2$'s geometry, its state ordering, and orbital character of the spin states are unchanged. State ordering and character can be used as key descriptors. On the basis of such descriptors, one would expect that a robust electronic structure would be equivalent to a robust magnetic behavior. Observation that is then confirmed by explicit calculation of SOC, magnetic anisotropy, and magnetic properties. Therefore, our calculations on $NiCp_2$ in different local environments confirm resilience of $NiCp_2$ magnetic behavior and support using $NiCp_2$ as a spin sensor. These results advance our understanding of magnetic behavior of molecular magnets on surface models that can be used as spin sensors.

This work on the $NiCp_2$ adsorption model is the first study using EOM-SF approaches for tackling such complex molecule/surface adducts. This has been possible by combining the SOC implementation of SF-TDDFT with the generality of the *ezMagnet* software, which can be interfaced with any method providing orbital angular momentum and SOCs. In addition, our approach has the advantage that it does not rely on spin-Hamiltonian formalism, selection of active space, or spin projections associated to the BS-DFT approach. Compared with periodic DFT+U, our SF-TDDFT protocol does not introduce additional system-dependent parameters apart from the ones already defining the exchange-correlation functional. Moreover, our approach does not apply periodic boundary conditions neither uses plane waves. Rather, it obtains reliable structures of $NiCp_2$ on the ionic MgO(001)

plane from a quantum mechanical cluster–point charges combined approach. The latter has the advantage to be able to investigate individual magnetic species when deposited on a surface without the need of large supercells. However, it has the limitation to be applicable to ionic surfaces only. However, chemical structures of nano-objects with metal substrates might be described well by DFT-based approaches. In this regard, the computational protocol implemented in the *ezMagnet* software has the potential to be combined (in addition to EOM-CC and SF-TDDFT) with density embedding formalism[90,91] (e.g., EOM-SF-CC-in-DFT or SF-TDDFT-in-DFT) allowing us to investigate electronic structure of magnetic species on metal surfaces.

We hope that our study will motivate further applications of SF-TDDFT combined with various embedding techniques to study even larger magnetic systems, and will inspire the development robust methodologies suitable for tackling complex electronic structures in extended structural models.

Acknowledgments

This work is supported by the Department of Energy through the DE-SC0018910 grant.

The authors declare the following competing financial interest(s): A.I.K. is the president and a part-owner of Q-Chem, Inc.

Supplementary material

Wave function analysis, basis-set effects, molar susceptibility within the Curie law, transition density matrix (TDM)-analysis of orbital angular momentum and spin–orbit matrix elements, explicit calculation of orbital angular momentum and spin–orbit coupling, nickelocene on the MgO surface, relevant Cartesian coordinates.

[1] Graham, M. J.; Zadrozny, J. M.; Fataftah, M. S.; Freedman, D. E. Forging solid-state qubit design principles in a molecular furnace *Chem. Mater.* **2017**, *29*, 1885–1897.

[2] Atzori, M.; Sessoli, R. The second quantum revolution: Role and challenges of molecular chemistry *J. Am. Chem. Soc.* **2019**, *141*, 11339–11352.

[3] Wasielewski, M. R.; Forbes, M. D. E.; Frank, N. L.; Kowalski, K.; Scholes, G. D.; Yuen-Zhou, J.; Baldo, M. A.; Freedman, D. E.; Goldsmith, R. H.; Goodson, T.; Kirk, M. L.; McCusker, J. K.; Ogilvie, J. P.; Shultz, D. A.; Stoll, S.; Whaley, K. B. Exploiting chemistry and molecular systems for quantum information science *Nature Rev. Chem.* **2020**, *4*, 490–504.

[4] Aravena, D.; Ruiz, E. Spin dynamics in single-molecule magnets and molecular qubits *Dalton Trans.* **2020**, *49*, 9916–9928.

[5] Zadrozny, J. M.; Niklas, J.; Poluektov, O. G.; Freedman, D. E. Millisecond coherence time in a tunable molecular electronic spin qubit *ACS Central Sci.* **2015**, *1*, 488–492.

[6] Divincenzo, D. P. The physical implementation of quantum computation *Fortschr. Phys.* **2000**, *48*, 2000.

[7] Bayliss, S. L.; Laorenza, D. W.; Mintun, P. J.; Kovos, B. D.; Freedman, D. E.; Awschalom, D. D. Optically addressable molecular spins for quantum information processing *Science* **2020**, *370*, 1309–1312.

[8] Bardin, J. C.; Slichter, D. H.; Reilly, D. J. Microwaves in quantum computing *IEEE Microw. Mag.* **2021**, *1*, 403–427.

[9] Heinrich, A. J.; Gupta, J. A.; Lutz, C. P.; Eigler, D. M. Single-atom spin-flip spectroscopy *Science* **2004**, *306*, 466–469.

[10] Tsukahara, N.; Noto, K.; Ohara, M.; Shiraki, S.; Takagi, N.; Takata, Y.; Miyawaki, J.; Taguchi, M.; Chainani, A.; Shin, S.; Kawai, M. Adsorption-induced switching of magnetic anisotropy in a single iron(II) phthalocyanine molecule on an oxidized Cu(110) surface *Phys. Rev. Lett.* **2009**, *102*, 167203.

[11] Rau, I. G.; Baumann, S.; Rusponi, S.; Donati, F.; Stepanow, S.; Gragnaniello, L.; Dreiser, J.; Piamonteze, C.; Nolting, F.; Gangopadhyay, S.; Albertini, O. R.; Macfarlane, R. M.; Lutz, C. P.; Jones, B. A.; Gambardella, P.; Heinrich, A. J.; Brune, H. Reaching the magnetic anisotropy limit of a 3d metal atom *Science* **2014**, *344*, 988–992.

[12] Cornia, A.; Mannini, M.; Sainctavit, P.; Sessoli, R. Chemical strategies and characterization tools for the organization of single molecule magnets on surfaces *Chem. Soc. Rev.* **2011**, *40*, 3076–3091.

[13] Yan, S.; Malavolti, L.; Burgess, J. A. J.; Droghetti, A.; Rubio, A.; Loth, S. Nonlocally sensing the magnetic states of nanoscale antiferromagnets with an atomic spin sensor *Sci. Adv.* **2017**, *3*, e1603137.

[14] Bachellier, N.; Ormaza, M.; Faraggi, M.; Verlhac, B.; Vérot, M.; Le Bahers, T.; Bocquet, M.-L.; Limot, L. Unveiling nickelocene bonding to a noble metal surface *Phys. Rev. B* **2016**, *93*, 195403.

[15] Ormaza, M.; Bachellier, N.; Faraggi, M. N.; Verlhac, B.; Abufager, P.; Ohresser, P.; Joly, L.; Romeo, M.; Scheurer, F.; Bocquet, M.; Lorente, N.; Limot, L. Efficient spin-flip excitation of a nickelocene molecule *Nano Lett.* **2017**, *17*, 1877–1882.

[16] Verlhac, B.; Bachellier, N.; Garnier, L.; Ormaza, M.; Abufager, P.; Robles, R.; Bocquet, M.-L.; Ternes, M.; Lorente, N.; Limot, L. Atomic-scale spin sensing with a single molecule at the apex of a scanning tunneling microscope *Science* **2019**, *366*, 623–627.

[17] Czap, G.; Wagner, P. J.; Xue, F.; Gu, L.; Li, J.; Yao, J.; Wu, R.; Ho, W. Probing and imaging spin interactions with a magnetic single-molecule sensor *Science* **2019**, *364*, 670–673.

[18] Czap, G.; Wagner, P. J.; Li, J.; Xue, F.; Yao, J.; Wu, R.; Ho, W. Detection of spin-vibration states in single magnetic molecules *Phys. Rev. Lett.* **2019**, *123*, 106803.

[19] Degen, C. L.; Reinhard, F.; Cappellaro, P. Quantum sensing *Rev. Mod. Phys.* **2017**, *89*, 035002.

[20] Yu, C.-J.; von Kugelgen, S.; d.W. Laorenza; Freedman, D. E. A molecular approach to quantum sensing *ACS Central Sci.* **2021**, *7*, 712–723.

[21] Malrieu, J. P.; Caballol, R.; Calzado, C. J.; de Graaf, C.; Guihéry, N. Magnetic interactions in molecules and highly correlated materials: Physical content, analytical derivation, and rigorous extraction of magnetic Hamiltonians *Chem. Rev.* **2013**, *114*, 429–492.

[22] Alessio, M.; Krylov, A. I. Equation-of-motion coupled-cluster protocol for calculating magnetic properties: Theory and applications to single-molecule magnets *J. Chem. Theory Comput.* **2021**, *17*, 4225–4241.

[23] Gozem, S.; Krylov, A. I. The ezSpectra suite: An easy-to-use toolkit for spectroscopy modeling *WIREs: Comput. Mol. Sci.* **2022**, *12*, e1546.

[24] Krylov, A. I. Equation-of-motion coupled-cluster methods for open-shell and electronically excited species: The hitchhiker's guide to Fock space *Annu. Rev. Phys. Chem.* **2008**, *59*, 433–462.

[25] Sneskov, K.; Christiansen, O. Excited state coupled cluster methods *WIREs: Comput. Mol. Sci.* **2012**, *2*, 566–584.

[26] Bartlett, R. J. Coupled-cluster theory and its equation-of-motion extensions *WIREs: Comput. Mol. Sci.* **2012**, *2*, 126–138.

[27] Krylov, A. I. Size-consistent wave functions for bond-breaking: The equation-of-motion spin-flip model *Chem. Phys. Lett.* **2001**, *338*, 375–384.

[28] Krylov, A. I. The spin-flip equation-of-motion coupled-cluster electronic structure method for a description of excited states, bond-breaking, diradicals, and triradicals *Acc. Chem. Res.* **2006**, *39*, 83–91.

[29] Casanova, D.; Krylov, A. I. Spin-flip methods in quantum chemistry *Phys. Chem. Chem. Phys.* **2020**, *22*, 4326–4342.

[30] Mayhall, N. J.; Head-Gordon, M. Computational quantum chemistry for single Heisenberg spin couplings made simple: Just one spin flip required *J. Chem. Phys.* **2014**, *141*, 134111.

[31] Mayhall, N. J.; Head-Gordon, M. Computational quantum chemistry for multiple-site Heisenberg spin couplings made simple: Still only one spin-flip required *J. Phys. Chem. Lett.* **2015**, *6*, 1982–1988.

[32] Orms, N.; Krylov, A. I. Singlet-triplet energy gaps and the degree of diradical character in binuclear copper molecular magnets characterized by spin-flip density functional theory *Phys. Chem. Chem. Phys.* **2018**, *20*, 13127–13144.

[33] Pokhilko, P.; Krylov, A. I. Effective Hamiltonians derived from equation-of-motion coupled-cluster wave-functions: Theory and application to the Hubbard and Heisenberg Hamiltonians *J. Chem. Phys.* **2020**, *152*, 094108.

[34] Berning, A.; Schweizer, M.; Werner, H.-J.; Knowles, P.; Palmieri, P. Spin-orbit matrix elements for internally contracted multireference configuration interaction wavefunctions *Mol. Phys.* **2000**, *98*, 1823–1833.

[35] Fedorov, D. G.; Koseki, S.; Schmidt, M. W.; Gordon, M. S. Spin-orbit coupling in molecules: Chemistry beyond the adiabatic approximation *Int. Rev. Phys. Chem.* **2003**, *22*, 551–592.

[36] Marian, C. M. Spin-orbit coupling and intersystem crossing in molecules *WIREs Comput.*

Mol. Sci. **2012**, *2*, 187–203.

[37] Schwerdtfeger, P., Ed. *Relativistic Electronic Structure Theory;* Elsevier, Amsterdam, 2002.

[38] Bethe, H. A.; Salpeter, E. E. *Quantum mechanics of one and two electron atoms;* Plenum: New York, 1977.

[39] Krylov, A. I.; Gill, P. M. W. Q-Chem: An engine for innovation *WIREs: Comput. Mol. Sci.* **2013**, *3*, 317–326.

[40] Epifanovsky, E.; Gilbert, T. B.; Feng, X.; Lee, J.; Mao, Y.; Mardirossian, N.; Pokhilko, P.; White, A. F.; Coons, M. P.; Dempwolff, A. L.; Gan, Z.; Hait, D.; Horn, P. R.; Jacobson, L. D.; Kaliman, I.; Kussmann, J.; Lange, A. W.; Lao, K. U.; Levine, D. S.; Liu, J.; McKenzie, S. C.; Morrison, A. F.; Nanda, K. D.; Plasser, F.; Rehn, D. R.; Vidal, M. L.; You, Z.-Q.; Zhu, Y.; Alam, B.; Albrecht, B. J.; Aldossary, A.; Alguire, E.; Andersen, J. H.; Athavale, V.; Barton, D.; Begam, K.; Behn, A.; Bellonzi, N.; Bernard, Y. A.; Berquist, E. J.; Burton, H. G. A.; Carreras, A.; Carter-Fenk, K.; Chakraborty, R.; Chien, A. D.; Closser, K. D.; Cofer-Shabica, V.; Dasgupta, S.; de Wergifosse, M.; Deng, J.; Diedenhofen, M.; Do, H.; Ehlert, S.; Fang, P.-T.; Fatehi, S.; Feng, Q.; Friedhoff, T.; Gayvert, J.; Ge, Q.; Gidofalvi, G.; Goldey, M.; Gomes, J.; González-Espinoza, C. E.; Gulania, S.; Gunina, A. O.; Hanson-Heine, M. W. D.; Harbach, P. H. P.; Hauser, A.; Herbst, M. F.; Hernández Vera, M.; Hodecker, M.; Holden, Z. C.; Houck, S.; Huang, X.; Hui, K.; Huynh, B. C.; Ivanov, M.; Jász, A.; Ji, H.; Jiang, H.; Kaduk, B.; Kähler, S.; Khistyaev, K.; Kim, J.; Kis, G.; Klunzinger, P.; Koczor-Benda, Z.; Koh, J. H.; Kosenkov, D.; Koulias, L.; Kowalczyk, T.; Krauter, C. M.; Kue, K.; Kunitsa, A.; Kus, T.; Ladjánszki, I.; Landau, A.; Lawler, K. V.; Lefrancois, D.; Lehtola, S.; Li, R. R.; Li, Y.-P.; Liang, J.; Liebenthal, M.; Lin, H.-H.; Lin, Y.-S.; Liu, F.; Liu, K.-Y.; Loipersberger, M.; Luenser, A.; Manjanath, A.; Manohar, P.; Mansoor, E.; Manzer, S. F.; Mao, S.-P.; Marenich, A. V.; Markovich, T.; Mason, S.; Maurer, S. A.; McLaughlin, P. F.; Menger, M. F. S. J.; Mewes, J.-M.; Mewes, S. A.; Morgante, P.; Mullinax, J. W.; Oosterbaan, K. J.; Paran, G.; Paul, A. C.; Paul, S. K.; Pavošević, F.; Pei, Z.; Prager, S.; Proynov, E. I.; Rák, A.; Ramos-Cordoba, E.; Rana, B.; Rask, A. E.; Rettig, A.; Richard, R. M.; Rob, F.; Rossomme, E.; Scheele, T.; Scheurer, M.; Schneider, M.; Sergueev, N.; Sharada, S. M.; Skomorowski, W.; Small, D. W.; Stein, C. J.; Su, Y.-C.; Sundstrom, E. J.; Tao, Z.; Thirman, J.; Tornai, G. J.; Tsuchimochi, T.; Tubman, N. M.; Veccham, S. P.; Vydrov, O.; Wenzel, J.; Witte, J.; Yamada, A.; Yao, K.; Yeganeh, S.; Yost, S. R.; Zech, A.; Zhang, I. Y.; Zhang, X.; Zhang, Y.; Zuev, D.;

Aspuru-Guzik, A.; Bell, A. T.; Besley, N. A.; Bravaya, K. B.; Brooks, B. R.; Casanova, D.; Chai, J.-D.; Coriani, S.; Cramer, C. J.; Cserey, G.; DePrince, A. E.; DiStasio, R. A.; Dreuw, A.; Dunietz, B. D.; Furlani, T. R.; Goddard, W. A.; Hammes-Schiffer, S.; Head-Gordon, T.; Hehre, W. J.; Hsu, C.-P.; Jagau, T.-C.; Jung, Y.; Klamt, A.; Kong, J.; Lambrecht, D. S.; Liang, W.; Mayhall, N. J.; McCurdy, C. W.; Neaton, J. B.; Ochsenfeld, C.; Parkhill, J. A.; Peverati, R.; Rassolov, V. A.; Shao, Y.; Slipchenko, L. V.; Stauch, T.; Steele, R. P.; Subotnik, J. E.; Thom, A. J. W.; Tkatchenko, A.; Truhlar, D. G.; Van Voorhis, T.; Wesolowski, T. A.; Whaley, K. B.; Woodcock, H. L.; Zimmerman, P. M.; Faraji, S.; Gill, P. M. W.; Head-Gordon, M.; Herbert, J. M.; Krylov, A. I. Software for the frontiers of quantum chemistry: An overview of developments in the Q-Chem 5 package *J. Chem. Phys.* **2021**, *155*, 084801.

[41] Pokhilko, P.; Epifanovsky, E.; Krylov, A. I. General framework for calculating spin–orbit couplings using spinless one-particle density matrices: theory and application to the equation-of-motion coupled-cluster wave functions *J. Chem. Phys.* **2019**, *151*, 034106.

[42] Pokhilko, P.; Krylov, A. I. Quantitative El-Sayed rules for many-body wavefunctions from spinless transition density matrices *J. Phys. Chem. Lett.* **2019**, *10*, 4857–4862.

[43] Carreras, A.; Jiang, H.; Pokhilko, P.; Krylov, A.I.; Zimmerman, P. M.; Casanova, D. Calculation of spin-orbit couplings using RASCI spinless one-particle density matrices: Theory and applications *J. Chem. Phys.* **2020**, *153*, 214107.

[44] Atanasov, M.; Ganyushin, D.; Pantazis, D. A.; Sivalingam, K.; Neese, F. Detailed ab initio first-principles study of the magnetic anisotropy in a family of trigonal pyramidal iron(II) pyrrolide complexes *Inorg. Chem.* **2011**, *50*, 7460–7477.

[45] Luzanov, A. V.; Sukhorukov, A. A.; Umanskii, V. E. Application of transition density matrix for analysis of excited states *Theor. Exp. Chem.* **1976**, *10*, 354–361; Russian original: Teor. Eksp. Khim., 10, 456 (1974).

[46] Luzanov, A. V.; Pedash, V. F. Interpretation of excited states using charge-transfer number *Theor. Exp. Chem.* **1979**, *15*, 338–341.

[47] Plasser, F.; Wormit, M.; Dreuw, A. New tools for the systematic analysis and visualization of electronic excitations. I. Formalism *J. Chem. Phys.* **2014**, *141*, 024106–13.

[48] Plasser, F.; Bäppler, S. A.; Wormit, M.; Dreuw, A. New tools for the systematic analysis and visualization of electronic excitations. II. Applications *J. Chem. Phys.* **2014**, *141*, 024107–12.

[49] Krylov, A. I. From orbitals to observables and back *J. Chem. Phys.* **2020**, *153*, 080901.

[50] Plasser, F.; Krylov, A. I.; Dreuw, A. libwfa: Wavefunction analysis tools for excited and open-shell electronic states *WIREs: Comput. Mol. Sci.* **2022**, *12*, e1595.

[51] Mewes, S.; Plasser, F.; Krylov, A.; Dreuw, A. Benchmarking excited-state calculations using exciton properties *J. Chem. Theory Comput.* **2018**, *14*, 710–725.

[52] Orms, N.; Rehn, D. R.; Dreuw, A.; Krylov, A. I. Characterizing bonding patterns in diradicals and triradicals by density-based wave function analysis: A uniform approach *J. Chem. Theory Comput.* **2018**, *14*, 638–648.

[53] Kotaru, S.; Käler, S.; Alessio, M.; Krylov, A. I. Magnetic exchange interactions in binuclear and tetranuclear iron(III) complexes described by spin-flip dft and Heisenberg effective Hamiltonians *J. Comput. Chem.* **2022;** in press, https://doi.org/10.1002/jcc.26941.

[54] Donati, F.; Rusponi, S.; Stepanow, S.; Wäckerlin, C.; Singha, A.; Persichetti, L.; Baltic, R.; Diller, K.; Patthey, F.; Fernandes, E.; Dreiser, J.; Šljivančanin, Ž.; Kummer, K.; Nistor, C.; Gambardella, P.; Brune, H. Magnetic remanence in single atoms *Science* **2016**, *352*, 318–321.

[55] Shao, Y.; Head-Gordon, M.; Krylov, A. I. The spin-flip approach within time-dependent density functional theory: Theory and applications to diradicals *J. Chem. Phys.* **2003**, *118*, 4807–4818.

[56] Bernard, Y. A.; Shao, Y.; Krylov, A. I. General formulation of spin-flip time-dependent density functional theory using non-collinear kernels: Theory, implementation, and benchmarks *J. Chem. Phys.* **2012**, *136*, 204103.

[57] Wang, F.; Ziegler, T. Time-dependent density functional theory based on a noncollinear formulation of the exchange-correlation potential *J. Chem. Phys.* **2004**, *121*, 12191.

[58] Valero, R.; Illas, F.; Truhlar, D. G. Magnetic coupling in transition-metal binuclear complexes by spin-flip time-dependent density functional theory *J. Chem. Theory Comput.* **2011**, *7*, 3523–31.

[59] Kotaru, S.; Krylov, A. I. **2022;** in preparation.

[60] Amos, A. T.; Hall, G. G. Single determinant wave functions *Phys. Rev. C* **1961**, *A 263*, 483.

[61] Luzanov, A. V. About V. Arnold's principle and its application to quantum chemistry and related fields *Kharkov University Bulletin; N. 1026 Chemical Series* **2012**, *21*.

[62] Bäppler, S. A.; Plasser, F.; Wormit, M.; Dreuw, A. Exciton analysis of many-body wave functions: Bridging the gap between the quasiparticle and molecular orbital pictures *Phys. Rev. A* **2014**, *90*, 052521.

[63] Plasser, F. Entanglement entropy of electronic excitations *J. Chem. Phys.* **2016**, *144*, 194107.

[64] Seiler, P.; Dunitz, J. D. The structure of nickelocene at room temperature and at 101 K *Acta Cryst.* **1980**, *B36*, 2255–2260.

[65] Prins, R.; van Voorst, J.D.W.; Schinkel, C.J. Zero-field splitting in the triplet ground state of nickelocene *Chem. Phys. Lett.* **1967**, *1*, 54–55.

[66] Baltzer, P.; Furrer, A.; Hulliger, J.; Stebler, A. Magnetic properties of nickelocene. A reinvestigation using inelastic neutron scattering and magnetic susceptibility *Inorg. Chem.* **1988**, *27*, 1543–1548.

[67] Guo, F.; Bar, A. K.; Layfield, R. A. Main group chemistry at the interface with molecular magnetism *Chem. Rev.* **2019**, *119*, 8479–8505.

[68] Evans, P.; Reta, D.; Whitehead, G. F.S.; Chilton, N. F.; Mills, D. P. Bis-monophospholyl dysprosium cation showing magnetic hysteresis at 48 K *J. Am. Chem. Soc.* **2019**, *141*, 19935–19940.

[69] Salzer, A.; Court, T.L.; Werner, H. Untersuchungen zur reaktivität von metall-π-komplexen: VII. Darstellung und eigenschaften kationischer cyclopentadienyl-diolefin-nickel-komplexe *J. Organomet. Chem.* **1973**, *54*, 325–330.

[70] Cleaves, P. A.; Ayres, A. J.; Vondung, L.; Stewart, J. C.; Cobb, P. J.; Wooles, A. J.; Liddle, S. T. Bridged and unbridged nickel–nickel bonds supported by cyclopentadienyl and phosphine ligand sets *Organometallics* **2020**, *39*, 4735–4746.

[71] Musgrave, R. A.; Hailes, R. L. N.; Annibale, V. T.; Manners, I. Role of torsional strain in the ring-opening polymerisation of low strain [*n*]nickelocenophanes *Chem. Sci.* **2019**, *10*, 9841–9852.

[72] Trtica, S.; Meyer, E.; Prosenc, M. H.; Heck, J.; Böhnert, T.; Görlitz, D. Naphthalene-bridged ansa-nickelocene: Synthesis, structure, electrochemical, and magnetic measurements *Eur. J. Inorg. Chem.* **2012**, *2012*, 4486–4493.

[73] Harriman, K. L.M.; Errulat, D.; Murugesu, M. Magnetic axiality: Design principles from molecules to materials *Trends Chem.* **2019**, *1*, 425–439.

[74] Downing, C. A.; Sokol, A. A.; Catlow, C. R. A. The reactivity of CO_2 on the MgO(100) surface *Phys. Chem. Chem. Phys.* **2014**, *16*, 184–195.

[75] Perdew, J.P.; Burke, K.; Ernzerhof, M. Generalized gradient approximation made simple *Phys. Rev. Lett.* **1996**, *77*, 3865–3868.

[76] Adamo, C.; Barone, V. Toward reliable density functional methods without adjustable parameters: The PBE0 model *J. Chem. Phys.* **1999**, *110*, 6158–6170.

[77] Rohrdanz, M.A.; Martins, K.M.; Herbert, J.M. A long-range-corrected density functional that performs well for both ground-state properties and time-dependent density functional theory excitation energies, including charge-transfer excited states *J. Chem. Phys.* **2009**, *130*, 054112.

[78] Alessio, M.; Bischoff, F. A.; Sauer, J. Chemically accurate adsorption energies for methane and ethane monolayers on the MgO(001) surface *Phys. Chem. Chem. Phys.* **2018**, *20*, 9760–9769.

[79] Alessio, M.; Usvyat, D.; Sauer, J. Chemically accurate adsorption energies: CO and H_2O on the MgO(001) surface *J. Chem. Theory Comput.* **2019**, *15*, 1329–1344.

[80] Dunning, Jr., T. H. Gaussian basis sets for use in correlated molecular calculations. I. The atoms boron through neon and hydrogen *J. Chem. Phys.* **1989**, *90*, 1007–1023.

[81] Woon, D. E.; Dunning, Jr., T. H. Gaussian basis sets for use in correlated molecular calculations. III. The atoms aluminum through argon *J. Chem. Phys.* **1993**, *98*, 1358–1371.

[82] Balabanov, N. B.; Peterson, K. A. Systematically convergent basis sets for transition metals. I. All-electron correlation consistent basis sets for the 3d elements Sc-Zn *J. Chem. Phys.* **2005**, *123*, 064107.

[83] Epifanovsky, E.; Zuev, D.; Feng, X.; Khistyaev, K.; Shao, Y.; Krylov, A. I. General implementation of resolution-of-identity and Cholesky representations of electron-repulsion integrals within coupled-cluster and equation-of-motion methods: Theory and benchmarks *J. Chem. Phys.* **2013**, *139*, 134105.

[84] Pokhilko, P.; Izmodenov, D.; Krylov, A. I. Extension of frozen natural orbital approximation to open-shell references: Theory, implementation, and application to single-molecule magnets *J. Chem. Phys.* **2020**, *152*, 034105.

[85] Pokhilko, P.; Epifanovskii, E.; Krylov, A. I. Double precision is not needed for many-body calculations: Emergent conventional wisdom *J. Chem. Theory Comput.* **2018**, *14*, 4088–4096.

[86] Head-Gordon, M. Characterizing unpaired electrons from the one-particle density matrix *Chem. Phys. Lett.* **2003**, *372*, 508–511.

[87] Vaara, J.; Rouf, S. A.; J, Mareš Magnetic couplings in the chemical shift of paramagnetic NMR *J. Chem. Theory Comput.* **2015**, *11*, 4840–4849.

[88] Kahn, O. *Molecular Magnetism;* VCH: New York, NY, 1993.

[89] El-Sayed, M. A. Spin–orbit coupling and the radiationless processes in nitrogen heterocycles

J. Chem. Phys. **1963**, *38*, 2834–2838.

[90] Prager, S.; Zech, A.; Aquilante, F.; Dreuw, A.; Wesolowski, T. A. First time combination of frozen density embedding theory with the algebraic diagrammatic construction scheme for the polarization propagator of second order *J. Chem. Phys.* **2016**, *144*, 204103.

[91] Parravicini, V.; Jagau, T.-C. Embedded equation-of-motion coupled-cluster theory for electronic excitation, ionization, electron attachment, and electronic resonances *Mol. Phys.* **2021**, *119*, e1943029.

TOC